Electronic Supplementary Material (ESI) for Sustainable Energy & Fuels.

Supporting Information

Chemically-tuned Cellulose Nanocrystals/Single Wall Carbon Nanosheet based Electrodes for Hybrid Supercapacitors

Nitesh Choudhary,[a,b] Shiva Singh,[a] Gaurav Malik,[b] Shakshi Bhardwaj,[a] Siddharth Sharma,[b] Akshay Tomar,[b] Sheetal Issar,[b] Ramesh Chandra,[*b] Pradip Kumar Maji[*a]

[a]*Department of Polymer and Process Engineering, Indian Institute of Technology Roorkee, Saharanpur Campus, Saharanpur- 247001, India*

[b]*Institute Instrumentation Centre, Indian Institute of Technology, Roorkee 247667, India*

******Corresponding author (s):* ***Ramesh Chandra, Pradip K. Maji***

Email: Ramesh.chandra@ic.iitr.ac.in, pradip@pe.iitr.ac.in

Contact No.: +91-9897031912, +91-7895965010

Supporting Information

Contents:

Supporting Information

Section S1: Extraction of chemically purified cellulose (CPC) and Cellulose nanocrystal (CNC) from raw *Saccharaum officinarum:*

S1.1 Chemically purified cellulose (CPC) extraction

The raw stems of Sugarcane bagasse were used to extract the cellulose through modified chlorite bleaching, followed by the NaOH treatment method. The synthesis of nanoscale cellulose particles from the raw source, *Saccharaum officinarum*, necessitates a series of pre-processing steps throughout the nanocellulose synthesis process as depicted in **Fig. S1.**[1] This process is aimed at producing high-quality nanocellulose with specific properties. The step-by-step extraction process is discussed below:

i. The raw materials of sugarcane bagasse undergo many cleaning processes, followed by drying in a hot air oven at 60 °C overnight, and finally, crushed for further process.

ii. Most extra, unstable, and easily dissolvable impurities are effectively eliminated. To remove dewax, the powder is subjected to a combination of ethanol and toluene in a 1:2 (v/v) ratio for 6-7 h with the use of a Soxhlet extractor.

iii. After dewax elimination, the product underwent delignification, wherein the lignin content was removed using a 5wt% $NaClO_2$ solution. A mixture of 25 g of $NaClO_2$, 2 ml of glacial acetic acid, and 0.5L of pre-heated distilled water with 10 g of dewaxed powder was dispersed to expedite the reaction.

iv. After shaking the mixture for 6h at 75 °C, the result was cleaned with distilled water (DW) and then vacuum-filtered. To eliminate chlorine complexes formed during the process of chlorite bleaching, a solution of 2wt% sodium sulfite is utilized on the vacuum-filtered product.

v. The sulfite-derived product underwent a bleaching process and was subsequently subjected to treatment with a 7wt% KOH solution.

vi. After vacuum-filtering and diluting the finished product with warm water, it attained a pH 7 which indicates neutrality. Therefore, chemically purified cellulose, also known as CPC, the resulted product was stored in a hot air furnace at a temperature of 60 °C. The detailed process description from raw to CNC extraction is shown in **Fig. S1.**

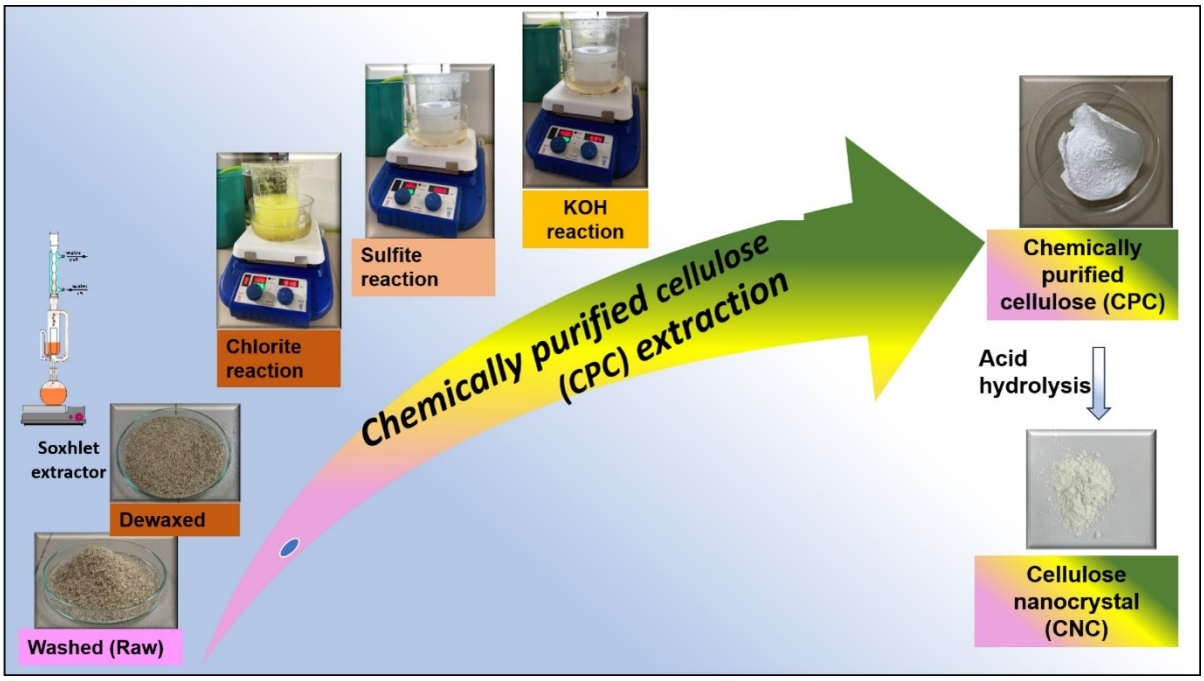

Fig. S1 A schematic representation of extraction of (CPC), chemically purified cellulose and Cellulose nanocrystals (CNC).

Supplementary section: S1.2

S1.2 Formation of Saccharum officinarum cellulose nanocrystals from Chemically purified cellulose, CPC

To the formation of cellulose nanocrystals (CNC), various methods can be employed to convert CPC into cellulose nanocrystals (CNC). These methods include acid hydrolysis using chemical techniques,[2] ongoing research and challenges in radical oxidation using enzymatic hydrolysis,[3] high-pressure homogenization,[4] ultrasonication, TEMPO (2, 2, 6, 6-Tetramethylpiperidine-1-yl) oxyl,[5] ball milling, and others. In this case, the CPC was converted into CNC through the acid hydrolysis process. The resultant dried CPC was immersed in a dimethyl sulfoxide (DMSO) solution to allow the fibres to expand, which would improve the chemical reactivity in the next steps. The swollen CPC was washed with distilled water (DW), filtered using vacuum pressure, and dried. The subsequent step involved the hydrolysis of CPC using a hydrochloric acid (4N HCl) solution. This process was conducted for a duration of 4h at a temperature of 55 °C, using a liquid-to-CPC ratio of 35:1. To quench the hydrolyzed CPC reaction, it was transferred to ice-cold water and allowed to settle for 24h, facilitating the separation of the CNC from the sugarcane bagasse suspension. Then, the excess acidic water

was removed, cautiously. **Fig. S2** provides the schematic illustration of the acid hydrolysis of CPC into CNC.

Furthermore, the CNC suspension was subjected to the bath sonicator operating at a frequency of 40 kHz, followed by a centrifugation process using the instrument REMI R-24 which was purchased from India, spinning at 8000 rpm for 18 minutes. The centrifugation steps were repeated 5-7 times in distilled and fresh water to wash the samples. The obtained residues were dialyzed against distilled water regularly until the water's pH was balanced. Next, using a probe sonicator made by Ningbo Sjia Lab Equipment (SKL 650D) Co., Ltd. in China, sound waves with an energy output of 20 kHz were applied to the dialyzed suspension for ten minutes. After being sonicated, the CNC suspensions were frozen for a day and then freeze-dried for 50 hours at -45 °C using a Lyophilizer made by M/S Operon in South Korea. The samples that had been freeze-dried were then kept for further analysis.

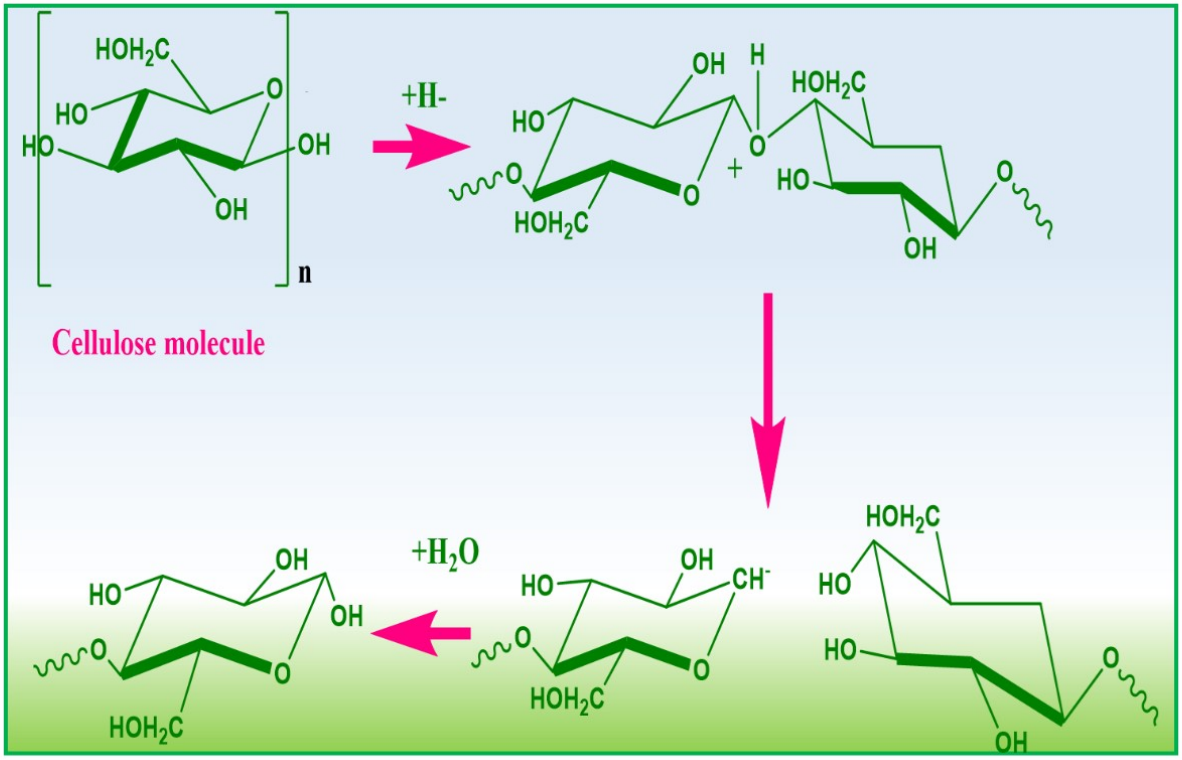

Fig. S2 A proposed mechanism of cellulose nanocrystals (CNC) acid hydrolysis.

Supplementary Section S2: Characterization details

S2.1 FTIR-ATR Spectra analysis

The removal of wax, lignin, hemicellulose, and the synthesis of CPC and CNC from sugarcane bagasse is demonstrated by the FTIR spectra of the samples acquired at each stage, as shown in **Fig. S3**. All the specimens showed a broad, strong peak at 3333 cm^{-1}, which is the result of the O–H stretching of cellulose's hydrogen-bonded hydroxyl groups. A broad change in transmittance corresponding to -OH stretching, including H-bonding, was observed in these spectra. The characteristic peaks located between 2900 and 2700 cm^{-1} indicate the C-H_n (n=1,2) stretching, and the chemical treatments are responsible for the transition from dewaxed to CPC.[6] Because the molecular structures of CPC and CNC are the same, their C-H_n stretching overlaps. The elimination of lignin following the chlorite and sulfite bleaching process is further verified by the loss of these characteristic peaks in the after-sulfite spectra, namely at 1516 and 1463 cm^{-1}, which are linked to aromatic C=C stretching.[7] Although the ester linkage (-COO-) has not vanished in the after-sulfite, the bleaching treatment had no discernible influence on the hemicellulose; however, the peak's strength decreased from the dewaxed to the after-sulfite.[8] Additionally, the hemicellulose was hydrolyzed by the alkali treatment, resulting in CPC. The full elimination of this peak at 1740 cm^{-1} in CPC, therefore, verifies the hemicellulose's removal. In addition, the samples from dewaxed to CNC exhibited these characteristic peaks at lengths of 1260, 1370, 1160, 1050, 900, and 1100–1030 cm^{-1}, which are indicative of native cellulose. Only the amorphous portion of the cellulose was destroyed by acid hydrolysis, producing crystalline cellulose, which will be further verified in the XRD section that follows.

S2.2 XRD analysis

The crystallinity of CNC and MACNC can be calculated using the Segal method. The crystallinity index (CI %) was quantitatively calculated by the Segal method by using eq.[9]

$$Crystanillity\ Index, C.I. = \frac{I_{200} - I_{am}}{I_{200}} \times 100$$

where I_{200} is the crystalline intensity of the (200) peak for cellulose at 22.7° 2θ, and I_{am} is the amorphous intensity at 18° 2θ for cellulose. From this method, the crystallinity index of CNC and MACNC has been observed at 61% and 56% respectively.

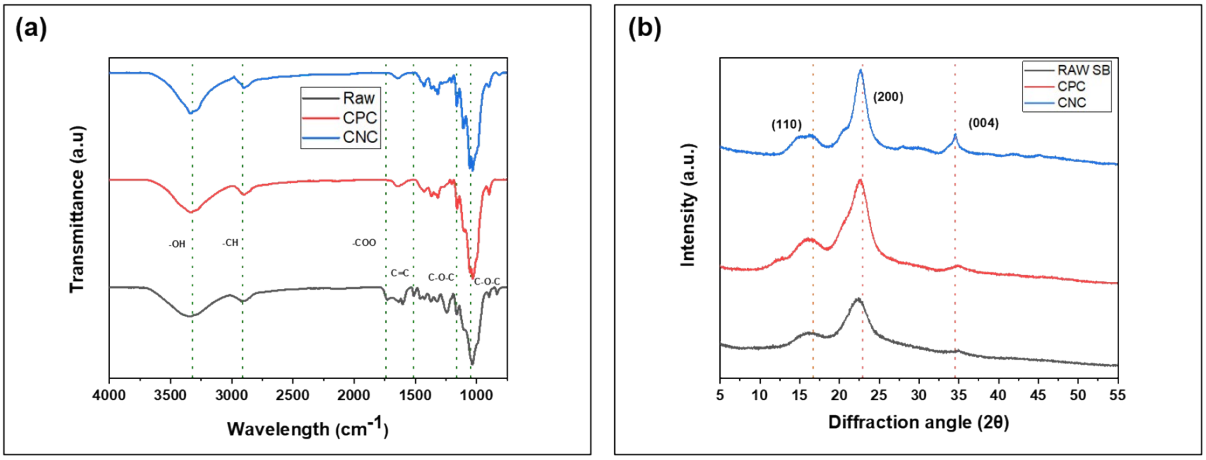

Fig. S3 (a) ATR-FTIR spectra (b) XRD spectra of raw, CPC (Chemically purified cellulose), CNC (Cellulose nanocrystal) of sugarcane bagasse.

S2.3 FESEM analysis:

The untreated fiber was initially dark brown. However, it changed to a lighter tone following dewaxing. The bleaching technique left the treated fibre completely white, indicating that cellulosic material made up the entirety of the fibre. Following chemical pre-treatments, these color variations showed that wax, lignin, pectin, hemicellulose, and other contaminants had been removed from raw pine.

After each phase, it is crucial to assess how the morphology is altered and analyze the structural alterations brought about in the crystals. FESEM micrographs were used to examine the surface morphology of the raw CPC, CNC, and CNT; and cross-section of the proposed electrode material i.e., 9wt% MACNC/CNT as shown in **Fig. S4,** the structure of the raw SB appears to be compact and smooth. The well-closed compact structure of raw could be attributed to an outer protective layer of non-cellulosic components such as oil, wax, Hemicellulose, etc., surrounding the bundles of Cellulose fibrils. It was observed that acidic bleaching had a profound influence on the microstructural properties as compared to the raw. After the acidified sodium chlorite reaction, the surface became rough and irregular. As a result of lignin's oxidation by chlorine at an acidic pH, lignin and other extractives became soluble and were removed, causing the development of fractures and micropores. It is observed that the FESEM of CNC shows crystalline imaging (rod-like morphology) as shown in the manuscript file.

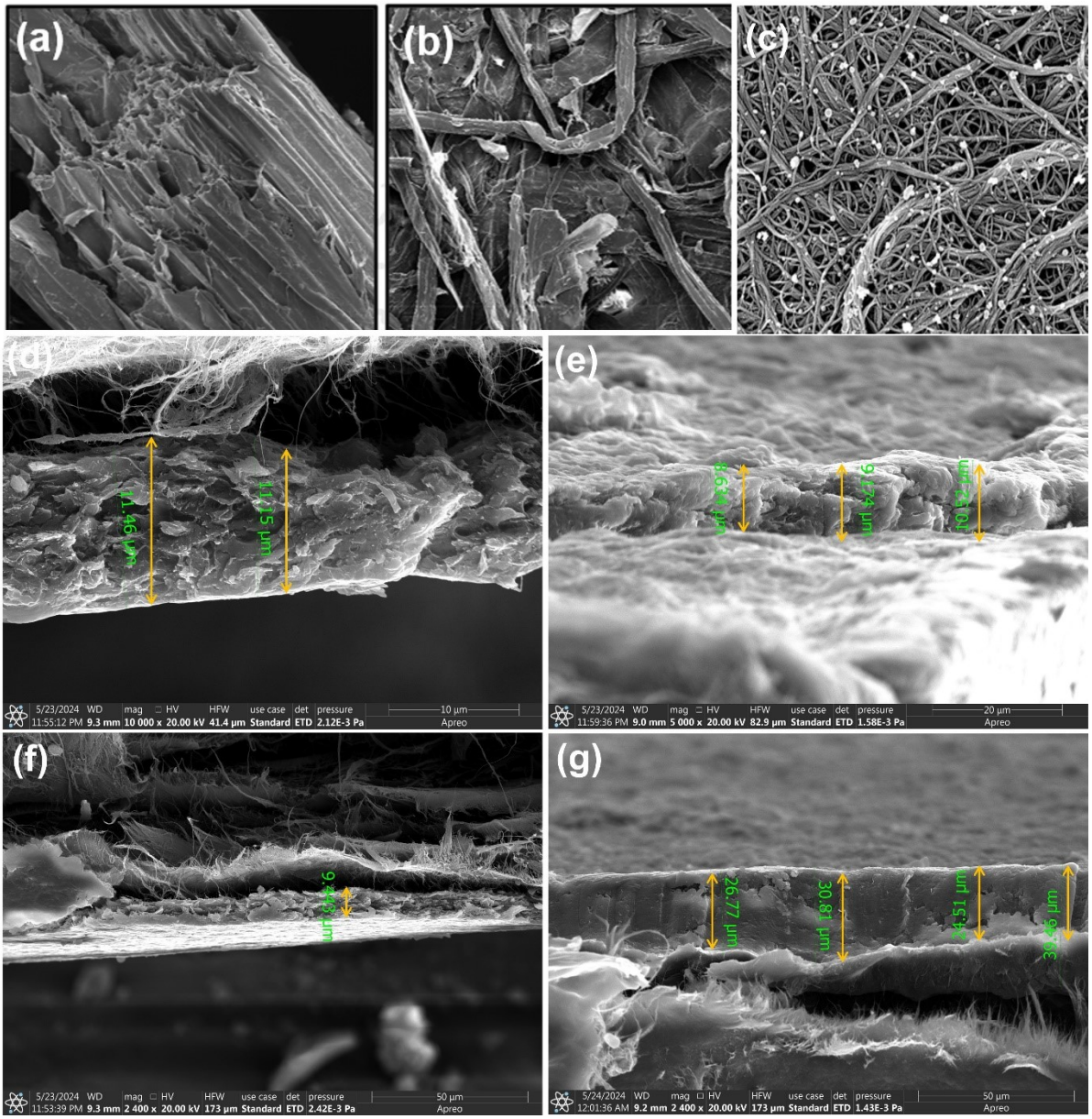

Fig. S4 shows the FESEM images of the (a) raw, (b) CPC, and (c) SWCNT sheet and (d-g) SEM Cross-section of 9wt% MACNC/CNT proposed electrode material.

S3 Calculation of electrochemical parameters

S3.1 Electrodes in three-electrode configuration.

The areal capacitance of the electrode,

$$C_a = \frac{2 \times I \times dt}{V \times A} \tag{S1}$$

Where C_a is the areal capacitance, td is the discharge time, I is the current density, V is the voltage window and A is the area of the electrode.

The energy density (E) and power density (P) were calculated using equation (S2 and S3) [10].

$$Energy\ density\ = \frac{C_a\ \times\ \triangle V^2}{2\times\ 3600} \times 1000 \quad \text{(S2)}$$

$$Power\ density\ = \frac{E\ \times 3600}{\triangle\ t} \quad \text{(S3)}$$

Where E and P represent the areal energy ($Whcm^{-2}$) and power density (Wcm^{-2}) of the electrode, V is the voltage window, C_a represents the areal capacitance, and $\triangle t$ is the discharging time. All the calculated electrochemical results from the CV/GCD curve are tabulated in the tables.

The amount of material deposited on the CNT film was calculated by measuring the weight of the SWCNT sheet film before and after the MACNC deposition. The weight percentage of MACNC ($W_{MACNC}\%$) was estimated using the following equation:

Mass loss:

$$W_{MACNC\%} = \frac{W_f - W_i}{W_f} \times 100\% \quad (S4)$$

Where W_i is the initial weight of the SWCNT film, and W_f is the final weight of the SWCNT film after MACNC deposition.

$$MACNC\% = \frac{0.03660 - 0.01126}{0.03660} \times 100\%$$

$$MACNC\% = 69.234\%$$

$$W_{MACNC} = w_f - w_i \quad (S5)$$

$$WMACNC = \ 25.34\text{mg}$$

Hence, the deposition of Maleic anhydride ($W_{MACNC}\%$) on the surface of the CNT sheet is ~70%, and active mass loading is 25.34mg on the surface of the CNT sheet.

Table S1 shows the Roughness, Skewness (R_{sk}), and Kurtosis values (R_{ku}) of the materials CNC, MACNC, SWCNT, CNC/CNT, and MACNC/CNT.

Name of the electrode	**Parameters**	**Values**
CNC	Roughness Skewness (R_{sk}) Kurtosis value (R_{ku})	4.97 nm 0.297 3.23

MACNC	Roughness Skewness (R_{sk}) Kurtosis value (R_{ku})	2.54 nm -0.087 3.98
SWCNT	Roughness	R_{max} 296 nm, 46.5 nm
	Skewness (R_{sk})	-0.105
	Kurtosis value (R_{ku})	3.33
CNC/CNT	Roughness	R_{max} 132 nm, 19.4 nm
	Skewness (R_{sk})	-0.201
	Kurtosis value (R_{ku})	3.14
MACNC/CNT	Roughness	R_{max} 106 nm, Rq 18.5 nm
	Skewness (R_{sk})	-0.304
	Kurtosis value (R_{ku})	2.51

Table S2 Calculated specific capacitance (C_S) at various scan rates with energy density and integrated area from the CV curve of the 3wt% MACNC/CNT electrode.

Scan rates (3wt% MACNC/CNT)	**Area**	**Capacitance (mF/cm^2)**	**Energy Density ($\mu Wh/cm^2$)**
0.01	0.00369	474.76602	94.9532
0.02	0.00703	421.62694	84.32539
0.05	0.1183	283.85108	56.77022
0.1	0.01283	153.93913	30.78783
0.5	0.0138	33.12246	6.62449

Table S3 Calculated specific capacitance (C_S) at various scan rates with energy density and integrated area from the CV curve of the 6wt% MACNC/CNT electrode.

Scan rates (6wt% MACNC/CNT)	**Area**	**Capacitance (mF/cm^2)**	**Energy Density ($\mu Wh/cm^2$)**
0.02	0.00919	551.152	110.2305

0.05	0.01248	299.42102	59.8842
0.1	0.0140	168.08019	33.61604
0.2	0.01512	90.69571	18.13914
0.5	0.01605	38.5264	7.70528

Table S4 Calculated specific capacitance (C_S) at various scan rates with energy density and integrated area from the CV curve of the 9wt% MACNC/CNT electrode.

Scan rates (9wt% MACNC/CNT)	**Area**	**Capacitance (mF/cm^2)**	**Energy Density (µWh/cm^2)**
0.01	0.00532	638.9299	127.786
0.02	0.00906	543.44243	108.688
0.05	0.01264	303.46244	60.6925
0.1	0.01408	169.00158	33.80032
0.2	0.01508	90.46439	18.09288

Table S5: Calculated specific capacitance (C_S) at various scan rates with energy density and integrated area from the CV curve of the 12wt% MACNC/CNT electrode.

Scan rates (12wt% MACNC/CNT)	**Gravimetric area**	**Capacitance (mF/cm^2)**	**Energy Density (µWh/cm^2)**
0.01	0.00413	495.3257	99.06514
0.02	0.0071	426.05372	85.21074
0.1	0.01401	168.0802	33.61604
0.2	0.01512	90.696	18.13914

0.5	0.01605	38.5264	7.70528

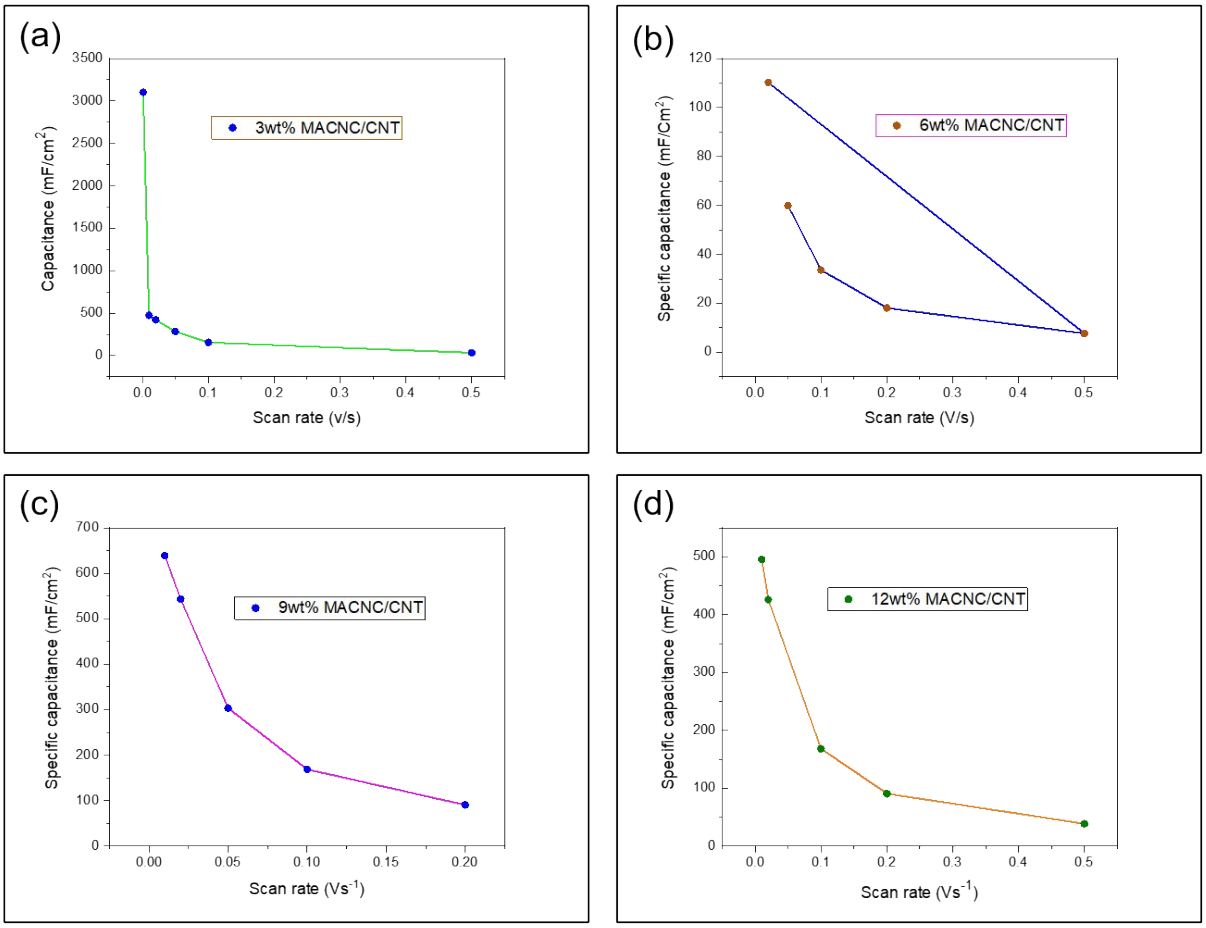

Fig. S5 Graphs between specific capacitance (mF/cm^2) vs. various scan rates (V/s) of (a) 3wt% MACNC electrode, (b) 6wt% MACNC electrode, (c) 9wt% MACNC electrode, and (d) 3wt% MACNC electrode.

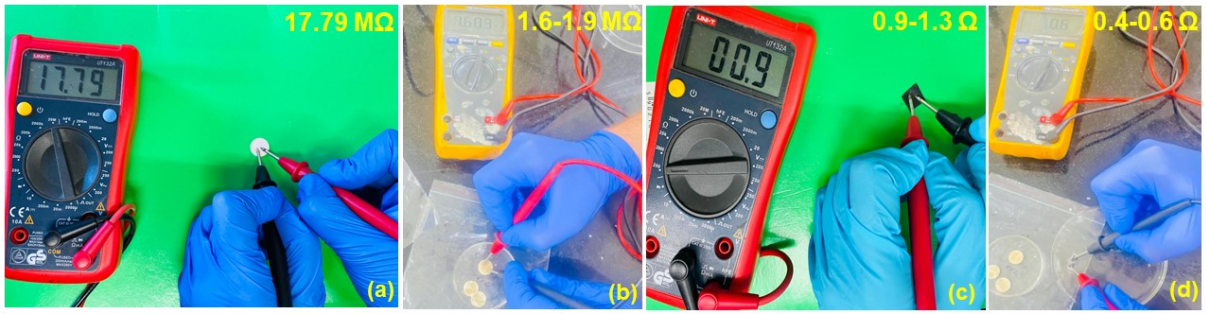

Name of the material	Resistance Observed (by Multimeter; Ω=Ohm, MΩ= Mega ohm)
(a): CNC (Cellulose nanocrystal)	17.79 MΩ
(b): MACNC (Maleic anhydride cellulose nanocrystal)	1.6-1.9 MΩ
(c): CNT (Carbon nanotube sheet)	0.9-1.3 Ω
(d): MACNC/CNT (Proposed material)	0.4-0.6 Ω

Electrode materials used	Specific capacitance (mF/cm^2)	Energy density ($\mu Wh/cm^2$)	Power density (m W/cm^2)	Current density or scan rate	Cyclic efficiency (%)	Cycles	Reference
CNF/Mxene (H_2SO_4)	25.3	0.08	0.145	2 mV s^{-1}	-	-	11
Free-standing cellulose electrode	522	94.7	0.573	5 mA cm^{-2}	94	2000	12
CNFs/Mxene/PC film	143	2.40	0.017	-	-	-	13

Fig. S6 Multimeter shows the electrical characteristics of material CNC, CNT, MACNC, and MACNC/CNT materials.

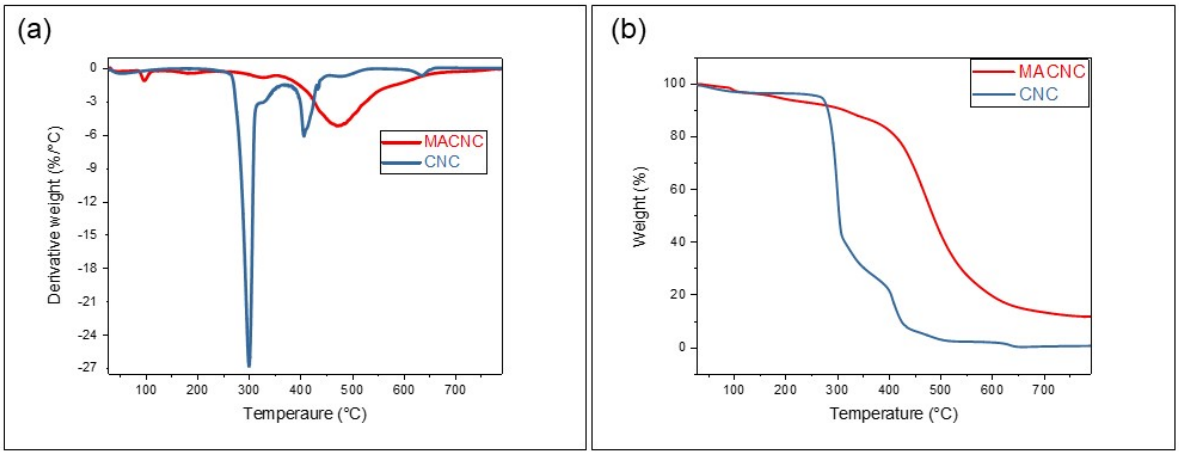

Fig. S7 Thermal stability – TGA and DTG curve of CNC and MACNC

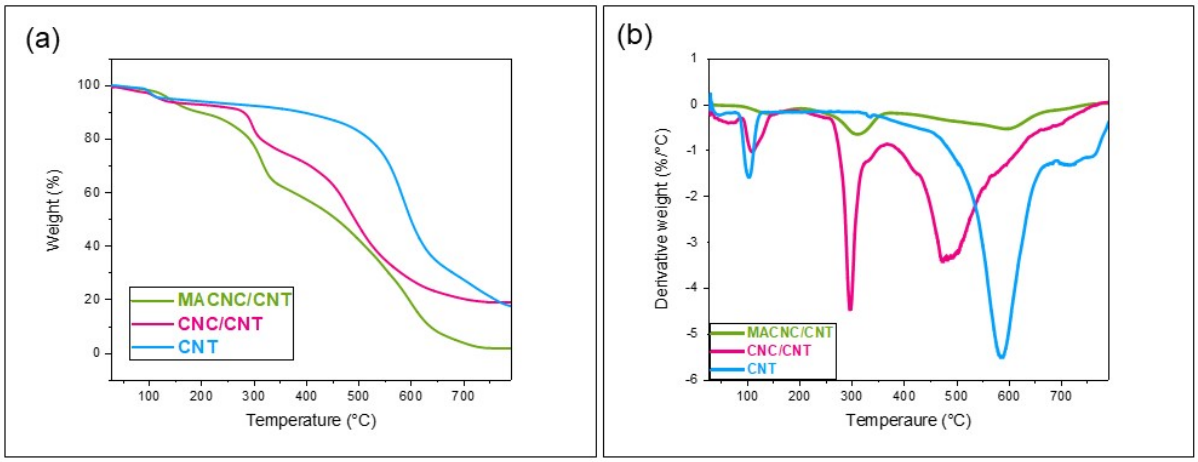

Fig. S8 Thermal stability – TGA and DTG curve of CNT (blue color), CNC/CNT (pink color), and MACNC/CNT (green color).

Table S6 Comparison of electrode materials used, areal specific capacitance, energy density, power density, scan rate or current denisties with cyclic efficiency after several cycles with the present study and other reported materials.

KOH							
PPy-coated KF (KF@PPy) PVA/H_2SO_4	1289	22.3	2.1	5 mV s^{-1}	97.4	2500	[14]
CNFs/RGO/BC paper (KOH)	810	110	27	10 mA cm^{-2}	99	10000	[15]
sLignin-O/S14 PVA/H_2SO_4 gel	53.2	450	1.6	0.08 mA c m^{-2}	81.3	8000	[16]
$ZnCl_2$ biochar	342	-	-	5 A g^{-1}	-	-	[17]
Wheat straw cellulosic biochar 1M KOH	0.3	-	-	0.5 A g^{-1}	-	-	[18]
Lignin-carbo/MoS_2 6M KOH	16	-	-	0.2 mA cm^{-2}	-	-	[19]
Biochar doped with PPy	370	-	-	-	72	1000	[20]
lignin/PAN membrane	11.5			0.5 mA cm^{-2}	92	5000	[21]
N-doped porous carbon fiber sheets from biomass-flax 6M KOH	703	-	-	20 mA cm^{-2}	-	-	[22]
Metal-like cellulose papers1 M Na_2SO_4	617	267.3	15.1	-	-	-	[23]
Bacterial cellulose composites (MXene@TOBC@PPy) PVA-H_2SO_4	928.9	142.6	0.197	0.7 mA cm^{-2}	85.5	5000	[24]
CNF/CNT/RGO carbon aerogels	109.4	-	-	0.4 mA cm^{-2}	83.8	100	[25]
9wt% MACNC/CNT hybrid composite 1M Li_2SO_4	1389.202	277.8403	12	5 m Vs^{-1}	76.4	12000	**Present work**

References

1 R. S. Meda, S. Jain, S. Singh, C. Verma, U. Nandi and P. K. Maji, *Ind Crops Prod*, , DOI:10.1016/j.indcrop.2022.115197.

2 S. Bhardwaj, S. Singh, R. S. Meda, S. Jain and P. K. Maji, *Biomass Convers Biorefin*, , DOI:10.1007/S13399-023-03970-Y.

3 B. Pereira and V. Arantes, *Ind Crops Prod*, , DOI:10.1016/J.INDCROP.2020.112377.

4 H. P. S. Abdul Khalil, Y. Davoudpour, M. N. Islam, A. Mustapha, K. Sudesh, R. Dungani and M. Jawaid, *Carbohydr Polym*, 2014, **99**, 649–665.

5 A. de Lima Pizi Cândido, N. F. Fregonezi, A. J. F. Carvalho, E. Trovatti and F. A. Resende, *Bionanoscience*, 2020, **10**, 766–772.

6 H. Yang, R. Yan, H. Chen, D. H. Lee and C. Zheng, *Fuel*, 2007, **86**, 1781–1788.

7 X. F. Sun, F. Xu, R. C. Sun, P. Fowler and M. S. Baird, *Carbohydr Res*, 2005, **340**, 97–106.

8 V. Gupta, D. Ramakanth, C. Verma, P. K. Maji and K. K. Gaikwad, *Biomass Convers Biorefin*, 2023, **13**, 15451–15462.

9 M. Beroual, L. Boumaza, O. Mehelli, D. Trache, A. F. Tarchoun and K. Khimeche, *J Polym Environ*, 2021, **29**, 130–142.

10 Q. Zhang, X. Wang, Z. Pan, J. Sun, J. Zhao, J. Zhang, C. Zhang, L. Tang, J. Luo, B. Song, Z. Zhang, W. Lu, Q. Li, Y. Zhang and Y. Yao, *Nano Lett*, 2017, **17**, 2719–2726.

11 Z. Liu, T. Lu and Q. Chen, *Carbon N Y*, 2021, **171**, 514–523.

12 T. Yuan, Z. Zhang, Q. Liu, X. T. Liu, Y. N. Miao and C. li Yao, *Carbohydr Polym*, 2023, **304**, 120519.

13 R. M. A. P. Lima, G. S. Dos Reis, M. Thyrel, J. J. Alcaraz-Espinoza, S. H. Larsson and H. P. de Oliveira, *Nanomaterials*, , DOI:10.3390/nano12050866.

14 J. Jyothibasu and R.-H. Lee, *Polymers (Basel)*, 2018, **10**, 1247.

15 L. Ma, R. Liu, H. Niu, L. Xing, L. Liu and Y. Huang, *ACS Applied Materials & Interfaces*, 2016, **8**, 33608–33618.

16 M. Yuan, F. Luo, Y. Rao, Y. Wang, J. Yu, H. Li and X. Chen, *J Power Sources*, 2021, **513**, 230558.

17 R. M. A. P. Lima, G. S. dos Reis, M. Thyrel, J. J. Alcaraz-Espinoza, S. H. Larsson and H. P. de Oliveira, *Nanomaterials*, 2022, **12**, 866.

18 U. Jamil, M. Zeeshan, S. R. Khan and S. Saeed, *Journal of Water Process Engineering*, 2023, **53**, 103892.

19 H. Chen, Z. Zhang, X. Zhong, Z. Zhuo, S. Tian, S. Fu, Y. Chen and Y. Liu, *J Hazard Mater*, 2021, **408**, 124847.

20 R. M. A. P. Lima, G. S. dos Reis, U. Lassi, E. C. Lima, G. L. Dotto and H. P. de Oliveira, *C (Basel)*, 2023, **9**, 59.

21 S. Wang, Y. Yu, S. Luo, X. Cheng, G. Feng, Y. Zhang, Z. Wu, G. Compagnini, J. Pooran and A. Hu, *Appl Phys Lett*, 2019, **115**, 083904.

22 D. He, L. Wu, Y. Yao, J. Zhang, Z. H. Huang and M. X. Wang, *Appl Surf Sci*, 2020, **507**, 145108.

23 Y. Ko, M. Kwon, W. K. Bae, B. Lee, S. W. Lee and J. Cho, *Nat Commun*, , DOI:10.1038/s41467-017-00550-3.

24 L. Fan, W. Zheng, Y. Yang, Y. Sun, S. Peng, J. Xu and G. Yin, *Cellulose*, 2023, **30**, 6507–6521.

25 H. Liu, T. Xu, C. Cai, K. Liu, W. Liu, M. Zhang, H. Du, C. Si and K. Zhang, *Adv Funct Mater*, , DOI:10.1002/adfm.202113082.